IEEE Access
Multidisciplinary | Rapid Review | Open Access Journal

Received September 11, 2019, accepted September 28, 2019, date of publication October 4, 2019, date of current version October 18, 2019.

Digital Object Identifier 10.1109/ACCESS.2019.2945604

Development of a Fault-Tolerant Permanent-Magnet Synchronous Motor

TONG FENG[1], SHUANGHUI HAO[1], XIUWEN ZHANG[1], TIANHONG YANG[1], AND LEI WANG[2]
[1]Harbin Institute of Technology, Harbin 150001, China
[2]Harbin University of Science and Technology, Harbin 150001, China

Corresponding author: Shuanghui Hao (156490479@qq.com)

ABSTRACT The failure of the motor or controller of a motor servo system could lead to terrible casualties and property loss in fields such as aviation and transportation. Current research mainly focuses on the algorithm for fault-tolerant control and the topological structure of hardware. Such approaches may reduce the system frequency through the use of a complex algorithm or increase the system cost through the use of special components. The present paper proposes and tests a multi-redundant, permanent-magnet synchronous motor. Through the parallel connection of multiple independent windings and a supporting control method that controls each redundancy separately, the system continues to run even when the winding or controller of one redundancy suffers an open-circuit or short-circuit fault. The system controller is easy to build and minimize without special components and does not require additional algorithms.

INDEX TERMS Fault-tolerant motor, multi-redundant, permanent magnet synchronous motor, proportional-integral control.

I. INTRODUCTION

Motor servo systems are widely used in the aviation and transportation industries. In these applications, serious casualties and property loss will occur if the servo system fails because of a fault. Therefore, the improvement of the reliability and fault-tolerance properties of servo motor system is an important research topic.

There is currently more research focus on the multi-phase permanent-magnet motor and switch reluctance motor in the field of fault-tolerant motors. The multi-phase permanent-magnet motor can keep running in the event of a failure through isolation of the fault phase and rebuilding of the control system. For example, a permanent-magnet synchronous motor (PMSM) with quadruple three-phase star-connected windings and a corresponding control algorithm was designed [1]. Because there are many phases, each phase has a lower proportion of the power, and the system thus ensures a rated torque output exceeding 50% when any winding has a symmetric short-circuit fault. The switch reluctance motor normally has no permanent magnet, winding or brush on the rotor and it thus has a lower failure rate. Each tooth of the stator has only one winding. Windings are energized by turns during working, and the independence of windings is thus high. It is thus easy to realize high-performance fault-tolerant control.

Research on the multi-phase permanent magnet motor has mainly focused on rebuilding the fault system and fault-tolerant control theory. Studies [2], [3] have used model predictive control and derived a prediction model for a specific fault situation according to the model of a healthy system, such that the normal decoupling transform can still be used after failure occurs. Other studies [4], [5] used a new frame of reference to build the running model and simplified the control after faults. Another study [6] proposed the orthogonal reduced-order transformation matrix based on fault-tolerant current. Other work [7] divided the vector space into six sectors and reconfigured six equal nonzero voltage vectors to achieve a new analogous three-phase space vector pulse width modulation (SVPWM) control.

Holt-per-Hertz (V/f) scalar control has been used to control the motor speed stably when the system suffers an open-circuit fault in one or two phases [8]. Meanwhile, a new method of phase current control has been proposed to maximize the reluctance torque [9]. Feedforward voltage compensation based on the short-circuit current and the back-electromotive force (back-emf) of the fault phase has been designed and used to eliminate the effect of short-circuit current [10]. Two fault-tolerant control strategies, involving the optimized copper loss and phase current, have been

The associate editor coordinating the review of this manuscript and approving it for publication was Sing Kiong Nguang.

proposed [11]. A current set that outputs the maximum smoothing torque by reconfiguring the maximum round magnetomotive force in different fault situations has been obtained [12].

Studies on the switched reluctance motor mainly focused on the topological structure and control of the power switch. One study [13] used four extra power switches and a relay network to keep the system working in the event of a fault. Another study [14] used a single-phase bridge to bypass the faulty part and form a fault-tolerant topology with the healthy part. Other work [15] optimized the position of the current sensor and suppressed short-circuit current by modifying the switching states of power transistors. Meanwhile, a system has been put into a derating state by shortening the conduction angle of the faulty phase and adjusting the duty cycle of all switches, thus suppressing the torque ripple caused by the short circuit [16]. Other work [17] identified the short switch using a logical dynamic model and analyzing system residual generation.

The references cited above show that research on the fault-tolerant motor mainly focuses on the system rebuild algorithm and fault-tolerant control after a fault occurs and the topological structure of hardware, such as the power switch or invertor part. The limitations are that an additional algorithm may increase the computing cost and decrease the system frequency and that a specific structure may need special components. Additionally, studies have mostly been conducted for one-phase or specific multi-phase failure.

Against the above background, the present paper proposes a multi-redundant PMSM that uses multiple independent windings and a supporting control method that controls each redundancy separately. When one redundancy's controller or winding is broken, the other redundancies allow the device to working normally and ensure that the whole system does not stop suddenly. This system does not need a complicated algorithm or specific components. Due to the parallel connection structure, the system also has a lower bus voltage, which reduces the effect on the power conversion unit. Furthermore, the control system can easily be downsized and integrated.

II. THEORETICAL ANALYSIS AND SIMULATION

A. ANALYSIS OF MUTUAL INDUCTANCE WINDING CONTROL

In contrast to a traditional PMSM, a multi-redundant PMSM system has mutual inductance between the stator windings of various redundancies. To realize this system, the current in mutual inductance windings must be shown to be controllable.

The voltage equilibrium of a mutual inductance winding under a static condition can be expressed as

$$\begin{cases} u_1 = R_1 i_1 + L_{s1}\dfrac{di_1}{dt} + L_m\dfrac{di_2}{dt} \\ u_2 = R_2 i_2 + L_{s2}\dfrac{di_1}{dt} + L_m\dfrac{di_2}{dt} \end{cases} \tag{1}$$

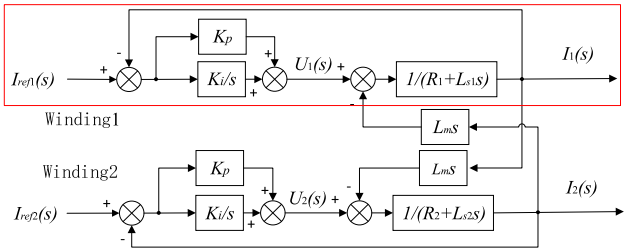

FIGURE 1. Block diagram of the current control system.

where R_1 and R_2 [Ω] are respectively the resistance of windings 1 and 2, L_{s1} and L_{s2} [H] are respectively the self-inductance of windings 1 and 2, and L_m [H] is the mutual inductance of windings 1 and 2.

Both windings 1 and 2 use a proportional–integral (PI) controller. Fig.1 is a block diagram of the current control system.

Expressions are obtained from Fig. 1 as

$$\begin{cases} U_1(s) = \left[I_{ref1}(s) - I_1(s)\right]\left(K_p + \dfrac{K_i}{s}\right) \\ U_2(s) = \left[I_{ref2}(s) - I_2(s)\right]\left(K_p + \dfrac{K_i}{s}\right) \end{cases} \tag{2}$$

For the multi-redundant PMSM in this paper, the parameters of different static windings and current references are the same, and the transfer function of the current loop can thus be written as

$$\frac{I_1(s)}{I_{ref}(s)} = \frac{I_2(s)}{I_{ref}(s)} = \frac{K_p s + K_i}{(L_m + L_s)s^2 + (K_p + R)s + K_i} \tag{3}$$

Equation (3) shows that the current control system is a second-order system. The standard expression of a second-order system is

$$G(s) = \frac{\omega_n^2}{s^2 + 2\xi\omega_n s + \omega_n^2} \tag{4}$$

where ω_n [Hz] is the system's natural frequency while ξ is the system's damping ratio.

From equations (3) and (4), the parameters for the PI controller are obtained as

$$\begin{cases} K_p = 2\xi\omega_n(L_m + L_s) - R \\ K_i = (L_m + L_s)\omega_n^2 \end{cases} \tag{5}$$

For a conventional PMSM, the block diagram of the current control system is shown in red in Fig. 1. The transfer function is

$$\frac{I_1(s)}{I_{ref}(s)} = \frac{K_p s + K_i}{L_s s^2 + (K_p + R)s + K_i} \tag{6}$$

From equations (4) and (6), the parameters of the PI controller are obtained as

$$\begin{cases} K_p = 2\xi\omega_n L_s - R \\ K_i = L_s\omega_n^2 \end{cases} \tag{7}$$

Equations (5) and (7) show that if regulating K_p and K_i and introducing L_m while calculating the parameters of the PI controller, ξ and ω_n of the mutual inductance winding are the same as those of conventional winding, which shows that current in a mutual inductance winding can be controlled as in conventional winding.

B. MATHEMATICAL MODEL FOR THE MULTI-REDUNDANT PMSM

The following assumptions are made before building a mathematical model of the motor.

1) Magnetic reluctance from the stator and rotor core, magnetic saturation, eddy currents, and hysteresis losses can be ignored.
2) The permeability of the permanent magnet is zero.
3) The rotor does not have a damping winding.
4) The magnetic field in the air gap has a normal distribution.
5) The effects of high harmonics can be ignored.

1) STATOR FLUX EQUATION

The flux of the stator winding is the sum of the armature magnetic field and rotor magnetic field. The rotor's excitation field axis is denoted as the d-axis, while the q-axis is 90 electrical degrees before the d-axis. The system uses the vector control strategy and $i_d = 0$. The system has n redundancies, and each redundancy's stator flux vector is decomposed on the d-axis and q-axis. The flux equation of each redundancy is, (8), as shown at the top of the next page, where $\psi_{d\mathrm{n}}$ and ψ_{qn} [Wb] are respectively the stator flux on the d-axis and q-axis of redundancy n, ψ_{fdn} and ψ_{fqn} [Wb] are respectively the rotor flux on the d-axis and q-axis of redundancy n, $L_{d\mathrm{n}}$ and L_{qn} [H] are respectively the self-inductance on the d-axis and q-axis of redundancy n, and $M_{dmq\mathrm{n}}$ and $M_{dnq\mathrm{m}}$ [H] are respectively the mutual inductance of the d-axis and q-axis of redundancies m and n. Further, M_{dmdn} [H] is the mutual inductance of the d-axes of redundancies m and n,M_{qmqn} [H] is the mutual inductance on the q-axis of redundancies m and n, and i_{dn} and i_{qn} are respectively the current components on the d-axis and q-axis of redundancy m.

The phases of different redundant windings are the same, and equation (8) can thus be rewritten as

$$\begin{cases} L_{d1} = L_{q1} = L_{d2} = L_{q2} = \cdots = L_{dn} = L_{qn} = L_s \\ M_{dmdn} = M_{dndm} = M_{qmqn} = M_{qnqm} = L_m \\ M_{dmqn} = M_{dnqm} = 0 \\ \psi_{fd1} = \psi_{fd2} = \cdots = \psi_{fdn} = \psi_{fd} \\ \psi_{fq1} = \psi_{fq2} = \cdots = \psi_{fqn} = 0 \end{cases} \tag{9}$$

where ψ_{fd} [Wb] is the rotor flux component on the d-axis, L_s [H] is the winding self-inductance, and L_m [H] is the mutual inductance of coaxial windings.

If the motor has three redundancies, then the stator flux equation is, (10), as shown at the top of the next page.

Equation (10) can be simplified as

$$\begin{cases} \psi_{d1} = \psi_{fd} \\ \psi_{q1} = L_s i_{q1} + L_m i_{q2} + L_m i_{q3} \\ \psi_{d2} = \psi_{fd} \\ \psi_{q2} = L_m i_{q1} + L_s i_{q2} + L_m i_{q3} \\ \psi_{d3} = \psi_{fd} \\ \psi_{q3} = L_m i_{q1} + L_m i_{q2} + L_s i_{q3} \end{cases} \tag{11}$$

2) STATOR VOLTAGE BALANCE EQUATION

The voltage vector equation of the stator is transformed from the a–b–c frame to the d–q frame through vector transformation as

$$u_s^{dq} = R_s i_s^{dq} + \frac{d\psi_s^{dq}}{dt} + j\omega_r \psi_s^{dq} \tag{12}$$

The voltage component equation then becomes

$$\begin{cases} u_d = R_s i_d + \frac{d\psi_d}{dt} - \omega_r \psi_q \\ u_q = R_s i_q + \frac{d\psi_q}{dt} + \omega_r \psi_d \end{cases} \tag{13}$$

where R_s [Ω] is the resistance of the d-axis and q-axis winding, ψ_d [Wb] is the flux vector component on the d-axis, ψ_q [Wb] is the flux vector component on the q-axis, and ω_r [rad/s] is the rotor speed.

After the stator flux equation is brought into equations (12) and (13), the voltage-equilibrium equation of the d–q axis of each redundancy can be obtained as, (14), as shown at the top of the next page.

When the motor has three redundancies, the voltage-equilibrium equation can be written as, (15), as shown at the top of the next page.

The resistances of the d-axis and q-axis windings for different redundancies are the same, and the known quantities can be brought into equation (15) to obtain

$$\begin{cases} u_{d1} = -\omega_r \left(L_s i_{q1} + L_m i_{q2} + L_m i_{q3} \right) \\ u_{q1} = R_s i_{q1} + L_s \frac{di_{q1}}{dt} + L_m \frac{di_{q2}}{dt} + L_m \frac{di_{q3}}{dt} + \omega_r \psi_{fd} \\ u_{d2} = -\omega_r \left(L_m i_{q1} + L_s i_{q2} + L_m i_{q3} \right) \\ u_{q2} = R_s i_{q2} + L_m \frac{di_{q1}}{dt} + L_s \frac{di_{q2}}{dt} + L_m \frac{di_{q3}}{dt} + \omega_r \psi_{fd} \\ u_{d3} = -\omega_r \left(L_m i_{q1} + L_m i_{q2} + L_s i_{q3} \right) \\ u_{q3} = R_s i_{q3} + L_m \frac{di_{q1}}{dt} + L_m \frac{di_{q2}}{dt} + L_s \frac{di_{q3}}{dt} + \omega_r \psi_{fd} \end{cases} \tag{16}$$

3) ELECTROMAGNETIC TORQUE EQUATION

When a PMSM uses vector control, its torque vector equation is

$$\begin{aligned} t_e &= p_0 \psi_s \times i_s = \mathrm{p}_0 \left(\psi_d + j\psi_q \right) \times \left(i_d + j i_q \right) \\ &= \mathrm{p}_0 \left(\psi_d i_q - \psi_q i_d \right) \end{aligned} \tag{17}$$

where p_0 is the number of pole pairs of the rotor, ψ_s [Wb] is the stator flux vector, and i_s [A] is the stator current vector.

After bringing equation (8) into (17), the torque equation of the multi-redundant motor becomes

$$t_e = p_0 \begin{bmatrix} \psi_{d1} \\ \psi_{d2} \\ \vdots \\ \psi_{dn} \end{bmatrix}^T \begin{bmatrix} i_{q1} \\ i_{q2} \\ \vdots \\ i_{qn} \end{bmatrix} - p_0 \begin{bmatrix} \psi_{q1} \\ \psi_{q2} \\ \vdots \\ \psi_{qn} \end{bmatrix}^T \begin{bmatrix} i_{d1} \\ i_{d2} \\ \vdots \\ i_{dn} \end{bmatrix} \tag{18}$$

$$\begin{bmatrix}\psi_{d1}\\ \psi_{q1}\\ \psi_{d2}\\ \psi_{q2}\\ \vdots\\ \psi_{dn}\\ \psi_{qn}\end{bmatrix}=\begin{bmatrix}L_{d1} & M_{d1q1} & M_{d1d2} & M_{d1q2} & \cdots & M_{d1dn} & M_{d1qn}\\ M_{q1d1} & L_{q1} & M_{q1d2} & M_{q1q2} & \cdots & M_{q1dn} & M_{q1qn}\\ M_{d2d1} & M_{d2q1} & L_{d2} & M_{d2q2} & \cdots & M_{d2dn} & M_{d2qn}\\ M_{q2d1} & M_{q2q1} & M_{q2d2} & L_{q2} & \cdots & M_{q2dn} & M_{q2qn}\\ \vdots & \vdots & \vdots & \vdots & \ddots & \vdots & \vdots\\ M_{dnd1} & M_{dnq1} & M_{dnd2} & M_{dnq2} & \cdots & L_{dn} & M_{dnqn}\\ M_{qnd1} & M_{qnq1} & M_{qnd2} & M_{qnq2} & \cdots & M_{qndn} & L_{qn}\end{bmatrix}\begin{bmatrix}i_{d1}\\ i_{q1}\\ i_{d2}\\ i_{2}\\ \vdots\\ i_{dn}\\ i_{qn}\end{bmatrix}+\begin{bmatrix}\psi_{fd1}\\ \psi_{fq1}\\ \psi_{fd2}\\ \psi_{fq2}\\ \vdots\\ \psi_{fdn}\\ \psi_{fqn}\end{bmatrix} \tag{8}$$

$$\begin{bmatrix}\psi_{d1}\\ \psi_{q1}\\ \psi_{d2}\\ \psi_{q2}\\ \psi_{d3}\\ \psi_{q3}\end{bmatrix}=\begin{bmatrix}L_{d1} & M_{d1q1} & M_{d1d2} & M_{d1q2} & M_{d1d3} & M_{d1q3}\\ M_{q1d1} & L_{q1} & M_{q1d2} & M_{q1q2} & M_{q1d3} & M_{q1q3}\\ M_{d2d1} & M_{d2q1} & L_{d2} & M_{d2q2} & M_{d2d3} & M_{d2q3}\\ M_{q2d1} & M_{q2q1} & M_{q2d2} & L_{q2} & M_{q2d3} & M_{q2q3}\\ M_{d3d1} & M_{d3q1} & M_{d3d2} & M_{d3q2} & L_{d3} & M_{d3q3}\\ M_{q3d1} & M_{q3q1} & M_{q3d2} & M_{q3q2} & M_{q3d3} & L_{q3}\end{bmatrix}\begin{bmatrix}i_{d1}\\ i_{q1}\\ i_{d2}\\ i_{q2}\\ i_{d3}\\ i_{q3}\end{bmatrix}+\begin{bmatrix}\psi_{fd1}\\ \psi_{fq1}\\ \psi_{fd2}\\ \psi_{fq2}\\ \psi_{fd3}\\ \psi_{fq3}\end{bmatrix} \tag{10}$$

$$\begin{aligned}\begin{bmatrix}u_{d1}\\ u_{q1}\\ u_{d2}\\ u_{q2}\\ \vdots\\ u_{dn}\\ u_{qn}\end{bmatrix}=&\begin{bmatrix}R_{d1}i_{d1}\\ R_{q1}i_{q1}\\ R_{d2}i_{d2}\\ R_{q2}i_{q2}\\ \vdots\\ R_{dn}i_{dn}\\ R_{qn}i_{qn}\end{bmatrix}+\frac{d}{dt}\begin{bmatrix}L_{d1} & M_{d1q1} & M_{d1d2} & M_{d1q2} & \cdots & M_{d1dn} & M_{d1qn}\\ M_{q1d1} & L_{q1} & M_{q1d2} & M_{q1d2} & \cdots & M_{q1dn} & M_{q1qn}\\ M_{d2d1} & M_{d2q1} & L_{d2} & M_{d2q2} & \cdots & M_{d2dn} & M_{d2qn}\\ M_{q2d1} & M_{q2q1} & M_{q2d2} & L_{q2} & \cdots & M_{q2dn} & M_{q2qn}\\ \vdots & \vdots & \vdots & \vdots & \ddots & \vdots & \vdots\\ M_{dnd1} & M_{dnq1} & M_{dnd2} & M_{dnq2} & \cdots & L_{dn} & M_{dnqn}\\ M_{qnd1} & M_{qnq1} & M_{qnd2} & M_{qnq2} & \cdots & M_{qndn} & L_{qn}\end{bmatrix}\begin{bmatrix}i_{d1}\\ i_{q1}\\ i_{d2}\\ i_{q2}\\ \vdots\\ i_{dn}\\ i_{qn}\end{bmatrix}+\frac{d}{dt}\begin{bmatrix}\psi_{fd1}\\ \psi_{fq1}\\ \psi_{fd2}\\ \psi_{fq2}\\ \vdots\\ \psi_{fdn}\\ \psi_{fqn}\end{bmatrix}\\ &+\omega_r\begin{bmatrix}-M_{q1d1} & -L_{q1} & -M_{q1d2} & -M_{q1q2} & \cdots & -M_{q1dn} & -M_{q1qn}\\ L_{d1} & M_{d1q1} & M_{d1d2} & M_{d1q2} & \cdots & M_{d1dn} & M_{d1qn}\\ -M_{q2d1} & -M_{q2q1} & -M_{q2d2} & -L_{q2} & \cdots & -M_{q2dn} & -M_{q2qn}\\ M_{d2d1} & M_{d2q1} & L_{d2} & M_{d2q2} & \cdots & M_{d2dn} & M_{d2qn}\\ \vdots & \vdots & \vdots & \vdots & \ddots & \vdots & \vdots\\ -M_{qnd1} & -M_{qnq1} & -M_{qnd2} & -M_{qnq2} & \cdots & -M_{qndn} & -L_{qn}\\ M_{dnd1} & M_{dnq1} & M_{dnd2} & M_{dnq2} & \cdots & L_{dn} & M_{dnqn}\end{bmatrix}\begin{bmatrix}i_{d1}\\ i_{q1}\\ i_{d2}\\ i_{q2}\\ \vdots\\ i_{dn}\\ i_{qn}\end{bmatrix}+\omega_r\begin{bmatrix}-\psi_{fq1}\\ \psi_{fd1}\\ -\psi_{fq2}\\ \psi_{fd2}\\ \vdots\\ -\psi_{fqn}\\ \psi_{fdn}\end{bmatrix}\end{aligned} \tag{14}$$

$$\begin{aligned}\begin{bmatrix}u_{d1}\\ u_{q1}\\ u_{d2}\\ u_{q2}\\ u_{d3}\\ u_{q3}\end{bmatrix}=&\begin{bmatrix}R_{d1}i_{d1}\\ R_{q1}i_{q1}\\ R_{d2}i_{d2}\\ R_{q2}i_{q2}\\ R_{d3}i_{d3}\\ R_{q3}i_{q3}\end{bmatrix}+\frac{d}{dt}\begin{bmatrix}L_{d1} & M_{d1q1} & M_{d1d2} & M_{d1q2} & M_{d1d3} & M_{d1q3}\\ M_{q1d1} & L_{q1} & M_{q1d2} & M_{q1q2} & M_{q1d3} & M_{q1q3}\\ M_{d2d1} & M_{d2q1} & L_{d2} & M_{d2q2} & M_{d2d3} & M_{d2q3}\\ M_{q2d1} & M_{q2q1} & M_{q2d2} & L_{q2} & M_{q2d3} & M_{q2q3}\\ M_{d3d1} & M_{d3q1} & M_{d3d2} & M_{d3q2} & L_{d3} & M_{d3q3}\\ M_{q3d1} & M_{q3q1} & M_{q3d2} & M_{q3q2} & M_{q3d3} & L_{q3}\end{bmatrix}\begin{bmatrix}i_{d1}\\ i_{q1}\\ i_{d2}\\ i_{q2}\\ i_{d3}\\ i_{q3}\end{bmatrix}+\frac{d}{dt}\begin{bmatrix}\psi_{fd1}\\ \psi_{fq1}\\ \psi_{fd2}\\ \psi_{fq2}\\ \psi_{fd3}\\ \psi_{fq3}\end{bmatrix}\\ &+\omega_r\begin{bmatrix}-M_{q1d1} & -L_{q1} & -M_{q1d2} & -M_{q1q2} & -M_{q1d3} & -M_{q1q3}\\ L_{d1} & M_{d1q1} & M_{d1d2} & M_{d1q2} & M_{d1d3} & M_{d1q3}\\ -M_{q2d1} & -M_{q2q1} & -M_{q2d2} & -L_{q2} & -M_{q2d3} & -M_{q2q3}\\ M_{d2d1} & M_{d2q1} & L_{d2} & M_{d2q2} & M_{d2d3} & M_{d2q3}\\ -M_{q3d1} & -M_{q3q1} & -M_{q3d2} & -M_{q3q2} & -M_{q3d3} & -L_{q3}\\ M_{d3d1} & M_{d3q1} & M_{d3d2} & M_{d3q2} & L_{d3} & M_{d3q3}\end{bmatrix}\begin{bmatrix}i_{d1}\\ i_{q1}\\ i_{d2}\\ i_{q2}\\ i_{d3}\\ i_{d3}\end{bmatrix}+\omega_r\begin{bmatrix}-\psi_{fq1}\\ \psi_{fd1}\\ -\psi_{fq2}\\ \psi_{fd2}\\ -\psi_{fq3}\\ \psi_{fd3}\end{bmatrix}\end{aligned} \tag{15}$$

For a PMSM with three redundancies, the electromagnetic torque equation is

$$\begin{aligned}t_e &= p_0\left(\psi_{d1}i_{q1}+\psi_{d2}i_{q2}+\psi_{d3}i_{q3}\right)\\ &= p_0\psi_{fd}(i_{q1}+i_{q2}+i_{q3})\end{aligned} \tag{19}$$

In the real world, controlling the motion of the load is the same as controlling the output torque of the motor. According to the dynamic principle, the equation of mechanical motion is

$$t_e = J\frac{d\omega_r}{dt}+R_\omega\omega_r+t_L = \mathrm{J}\frac{d^2\theta_r}{dt^2}+R_\omega\frac{d\theta_r}{dt}+t_L \tag{20}$$

where t_e [N·m] is the motor output torque, t_L [N·m] is the load torque, J [kg·m^2] is the rotational inertia, ω [rad/s] is the mechanical angular velocity of the rotor, R_ω [N·m·s/rad] is the

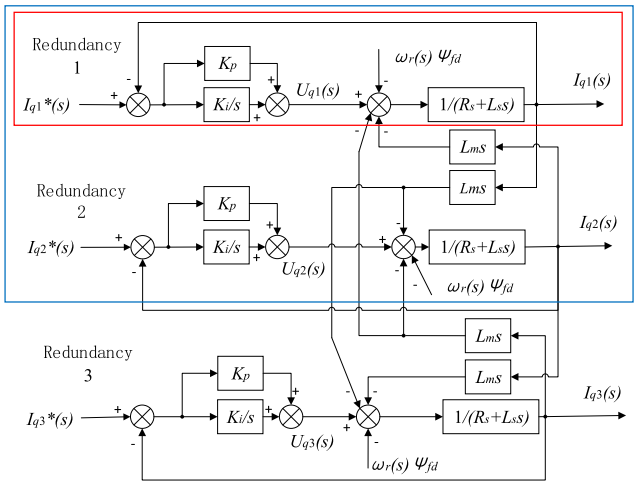

FIGURE 2. Control block diagram for current on the q-axis.

damping coefficient, and θ_r [rad] is the angular displacement of the rotor.

Equation (20) shows that the control of both the angular velocity and angular displacement is realized by controlling the torque $(t_e - t_L)$. Thus, improving the control quality of electromagnetic torque will improve the performance of the whole PMSM system.

C. ANALYSIS OF THE MULTI-REDUNDANT CONTROL SYSTEM

A vector control strategy was used for the new motor. To realize good control performance, this system uses two loop PI controllers, including a current loop and velocity loop. Equation (20) shows that to control the motor output torque is to control the current on the q-axis of each redundancy. Fig. 2 is a control block diagram for current on the q-axis for a PMSM with three redundancies.

In Fig. 2, i_{q1}^*, i_{q2}^*, and i_{q3}^* are the reference current outputs from the host computer and i_{q1}, i_{q2}, and i_{q3} are the actual current in each of the three redundancies.

During operation, the response of the current loop is much faster than the mechanical response; thus, $\omega_r \psi_{fd}$ can be treated as constant and ignored when calculating the system's transfer function. The working conditions of a PMSM with three redundancies can be divided into three situations.

When the system operates normally, the transfer function can be expressed as

$$G(s) = \frac{I_{q1}(s)}{I_q^*(s)} = \frac{I_{q2}(s)}{I_q^*(s)} = \frac{I_{q3}(s)}{I_q^*(s)} = \frac{K_p s + K_i}{(2L_m + L_s)s^2 + (K_p + R_s)s + K_i} \tag{21}$$

Equation (21) shows that the system is of second order, and the parametric expression of the PI controller is

$$\begin{cases} K_i = (L_s + 2L_m)\omega_n^2 \\ K_p = 2\xi\omega_n(L_s + 2L_m) - R_s \end{cases} \tag{22}$$

When one of the redundancies fails owing to a fault, the current control block is configured as the block within the blue rectangle in Fig. 2. The transfer function is

$$G(s) = \frac{I_{q1}(s)}{I_q^*(s)} = \frac{I_{q2}(s)}{I_q^*(s)} = \frac{K_p s + K_i}{(L_m + L_s)s^2 + (K_p + R_s)s + K_i} \tag{23}$$

The system is still of second order and its parametric expression is

$$\begin{cases} K_i = (L_s + L_m)\omega_n^2 \\ K_p = 2\xi\omega_n(L_s + L_m) - R_s \end{cases} \tag{24}$$

When two of the redundancies fail, the current control block is configured as shown by the block within the red rectangle in Fig. 2. The transfer function is

$$G(s) = \frac{K_p s + K_i}{L_s s^2 + (R_s + K_p)s + K_i} \tag{25}$$

The system is still of second order system and its parametric expression is

$$\begin{cases} K_i = L_s\omega_n^2 \\ K_p = 2\xi\omega_n L_s - R_s \end{cases} \tag{26}$$

In the equations above, L_m, L_s, and R_s are constants. Therefore, no matter which situation the system is working in, proper values for K_p and K_i allow the pole of the system to remain on the left side of the complex plane and the system to be stable. If the system is initially stable, any stray current will not change the denominator of the transfer function, and the system thus remains stable during faults.

D. SIMULATION BASED ON MATLAB AND SIMULINK

A mathematical model of the multi-redundant PMSM was used to build a simulation model in Simulink, as shown in Fig. 3. The inputs of the PMSM are voltages U_{q1}, U_{q2}, and U_{q3} on the three redundant q-axes and PMSM load t_L. The outputs are currents i_{q1}, i_{q2}, and i_{q3} for the three redundancies, rotational speed ω_r, and output torque t_e.

Fig.4 shows the PMSM control system model in Simulink. The inputs are the command speed ω and motor load t_L; the outputs are the same as those of the PMSM.

The basic parameters of the PMSM are listed in Table 1.

To simulate an operating situation in which two redundant windings fail, the simulation time was set to 5 s, the rotational speed was 30 rad/s, and the motor load was 30N · m. When t = 2 s, redundancy 3 was cut off, and when t = 4 s, redundancy 2 was cut off. The system response is shown in Figs. 5, 6, and 7.

Fig. 5, 6, and 7 show that when the system was initially working normally, the three-phase current waveforms for the three redundancies were the same, revealing that the current was synchronized. When redundancy 3 was cut off at t = 2 s, the current from redundancy 3 decreased to zero and the current from redundancies 1 and 2 increased to 1.5 times the

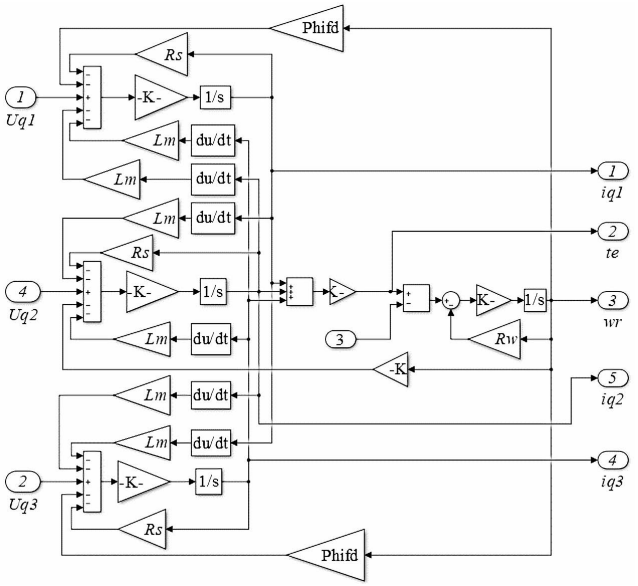

FIGURE 3. Simulation model of the PMSM with three redundancies.

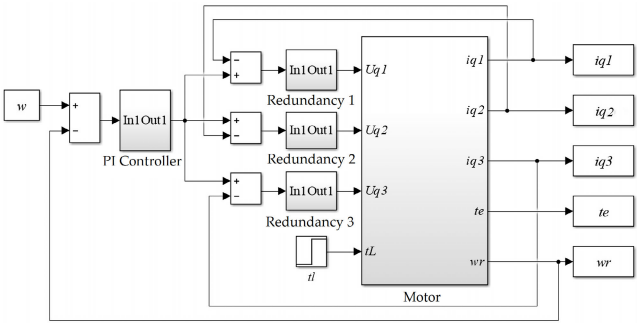

FIGURE 4. Simulation model of the control system for the PMSM with three redundancies.

TABLE 1. Basic parameters of the simulation model.

PARAMETER	POLE-PAIR NUMBER P_0	WINDING RESISTANCE $R_S(\Omega)$	SELF-INDUCTANCE L_S(MH)	MUTUAL INDUCTANCE L_M(MH)
Value	1	2.5	0.444	0.434
PARAMETER	ROTATIONAL INERTIA J(KG·M^2)	DAMPING COEFFICIENT R_W(N•S)	D-AXIS ROTOR FLUX Ψ_{FD}(WB)	
Value	2	0.01	1.00	

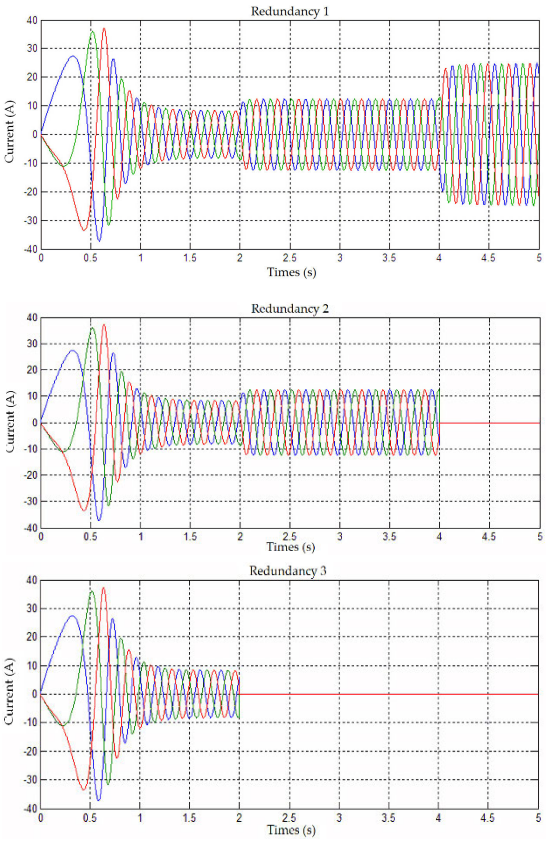

FIGURE 5. Current waveforms of U, V, and W for all three redundancies during the failure of two redundancies.

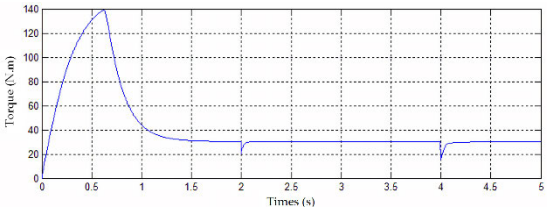

FIGURE 6. Motor output torque during the failure of two redundancies.

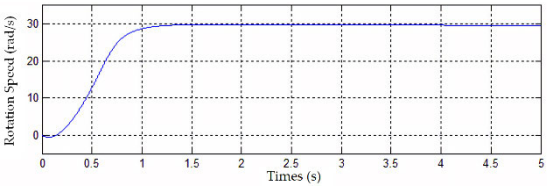

FIGURE 7. Motor speed during the failure of two redundancies.

synchronous current value. When redundancy 2 was also cut off at t = 4 s, the current from redundancy 2 decreased to zero and the current from redundancy 1 increased to twice the value of the synchronous current.

Because of the initial static friction of the motor, the torque was higher when the system started and then decreased to a value that matched the load stably. When redundancies 2 and 3 were cut off, the torque decreased slightly and then again quickly increased to a value that matched the load stably. The output torque was essentially constant during the entire process. The rotational speed increased rapidly to 30 rad/s. When redundancies 2 and 3 were cut off, the speed was maintained at the set value.

The simulations show that when any redundant system is cut off, the other redundancies transition from normal

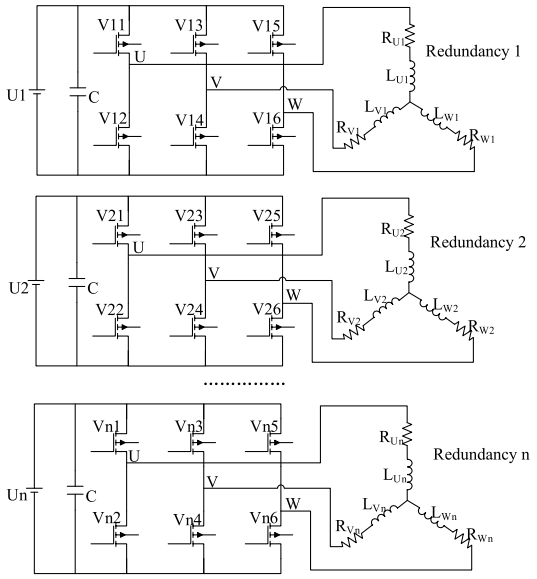

FIGURE 8. Basic theory of the multi-redundant motor.

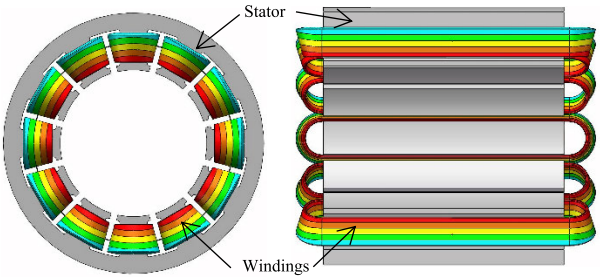

FIGURE 9. Schematic figure of stator windings.

operation to a compensation mode to increase the current automatically and maintain a constant output torque and speed.

III. DESIGN OF THE MOTOR AND CONTROLLER

A. DESIGN OF THE MULTI-REDUNDANT PMSM

1) MOTER STRUCTURE AND MATERIALS

The multi-redundant motor system has n sets of driver and stator winding. Each set is defined as one redundancy, and each redundancy has the same characteristics. All redundancies are in parallel with one another, and the sum of the output torques of all redundancies is the output torque of the motor. The basic theory of the multi-redundant motor is presented as Fig. 8.

Windings of different redundancies have the same enwinding method and same phase. There is physical isolation and thermal isolation between different redundancies. Magnetic field coupling still exists at present. Fig.9 is a schematic figure of the stator windings, where different colors indicate different redundancies.

Technical specifications of the motor designed in this study are given in Table 2.

Because of the higher load torque, the permanent magnetic material needs to have excellent magnetic properties, such as higher remanent magnetic induction, a maximum magnetic energy product, and coercivity, to give the motor higher energy density. Among common kinds of permanent magnetic material, Nd-Fe-B has a remanent magnetic induction as high as 1.49 T, maximum magnetic energy product up to 422 kJ/m^3, and coercivity of up to 1035 kA/m. Therefore, Nd-Fe-B, grade N38SH, was chosen as the magnetic material of the motor. The stator was made from 50W470 silicon steel and the rotor from #10 steel.

TABLE 2. Main PMSM specifications.

SPECIFICATION	VALUE	SPECIFICATION	VALUE
Power(kW)	6.3	AC Supply Voltage (V)	220
Max Speed(r/min)	100	Motor's quality(kg)	60
Torque(N·m)	600	Limit Torque(N·m)	650

2) STRUCTURAL DESIGN OF THE ROTOR AND PERMANENT MAGNET

The motor structure is that of an outer rotor. Because of the rotor's limited volume, the magnetic circuit structure is surface mounted. Surface-mounted structures can be divided into protrusion and insertion types.

A permanent magnet's differential permeability is approximately 1 and close to that of air, and the d-axis inductance of the protrusion type of structure is thus almost equal to the q-axis inductance; this type of structure is suitable for the control strategy of $i_d = 0$. In addition, the protrusion type of structure is simple and has low processing cost. A protrusion type rotor was therefore used in this study.

The motor used fan-shaped permanent magnets. The length of the magnetizing direction h_M strongly affects the d-axis reactance X_{ad}, and h_M can be approximately determined as

$$h_M = \frac{\mu_r}{\frac{B_r}{B_\delta} - 1}\delta_i \tag{27}$$

where μ_r [H/m] is the differential permeability of the permanent magnet, δ_i [mm] is the length of the motor air gap, B_r [T] is the remanent magnetic induction, B_δ [T] is the air gap flux density, and $\frac{B_r}{B_\delta}$ is the ratio of induction to flux density, normally set in the range of 1.1–1.35.

The N38SH permanent magnet has a remanent magnetic induction of 1.24 T. The maximum value of the air gap flux density was obtained as 1.06 T after simulation. The length of the motor air gap was taken as 1 mm. Inserting these values into equation (27) gives h_M as 6 mm.

When the motor's armature diameter, current density, and air-gap magnetic flux density are invariant, increasing the number of motor slot poles reduces the amount of copper and improves the motor's power density. However, it also increases the fabrication difficulty and makes it difficult to guarantee machining precision. After careful consideration,

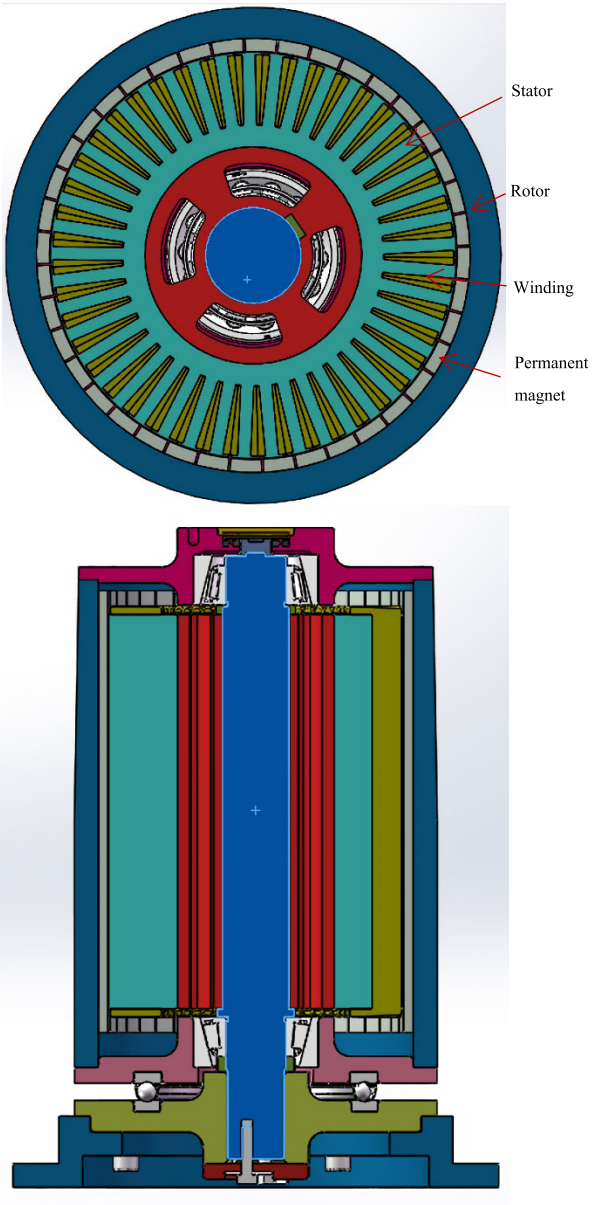

FIGURE 10. Three-dimensional structure of the multi-redundant motor.

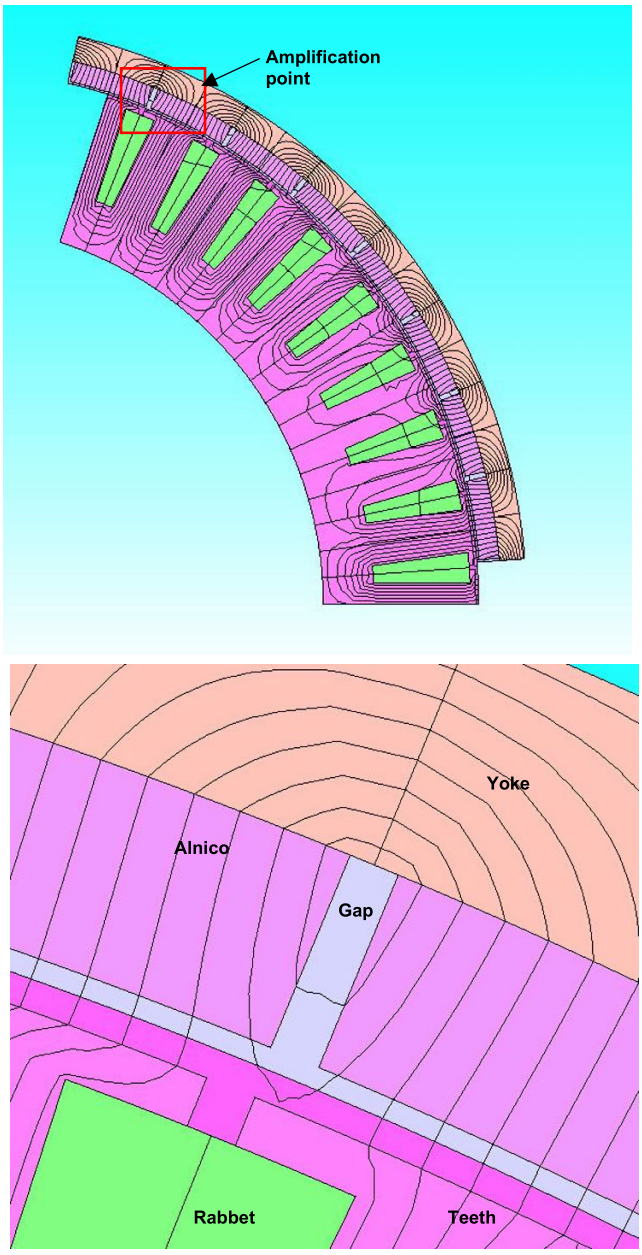

FIGURE 11. Magnetic lines of the prototype motor: (top) main diagram and (bottom) enlarged view of the air gap area.

this study chose 45 slots and 40 poles as the motor's plan. Fig. 10. shows the three-dimensional structure of the motor.

3) SIMULATION OF ELECTROMAGNETIC PROPERTIES

The armature winding in the present study adopted a Y connection. Variations in output characteristics and magnetic flux density were analyzed by changing the current magnitude.

Diagrams of the final magnetic force lines are shown in Fig.11. The top diagram shows that most magnetic force lines form closed loops through the teeth, air gaps, magnetic steel, and yokes, and these lines form the main magnetic flux. An enlarged diagram of the air gap area in the bottom panel shows that a small number of magnetic force lines do not pass through the teeth or yokes—these lines are the leakage magnetic flux. Fig.11. shows that there is little leakage flux and that the motor therefore has lower loss.

Fig.12. shows that the cogging torque of the motor fluctuated between $+1.14$ and -1.10 N·m, accounting for 0.37% of the specified torque, which meets the design requirements.

The output torque of the motor working at 500 ampere-turns is shown in Fig.13. The average output torque is 645.6 N·m, which is 7.6% more than the specified torque; the fluctuation of the torque is 18.5 N·m, accounting for 3.1% of the total output, which meets the design requirements.

The air-gap flux density variation is shown in Fig. 14. The result was processed with a fast Fourier transform, and the harmonics are shown in Fig. 15. The results show that

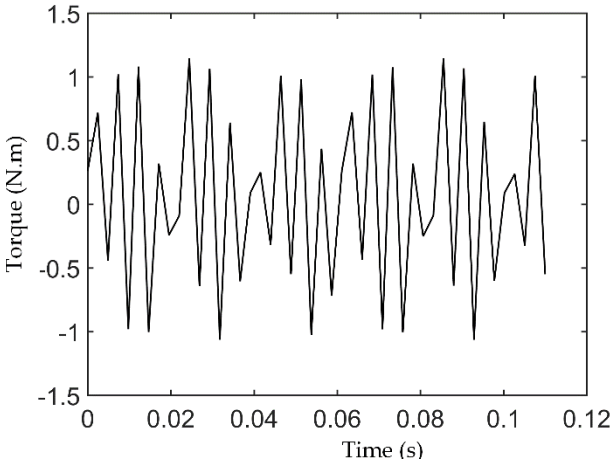

FIGURE 12. Cogging torque of the prototype motor.

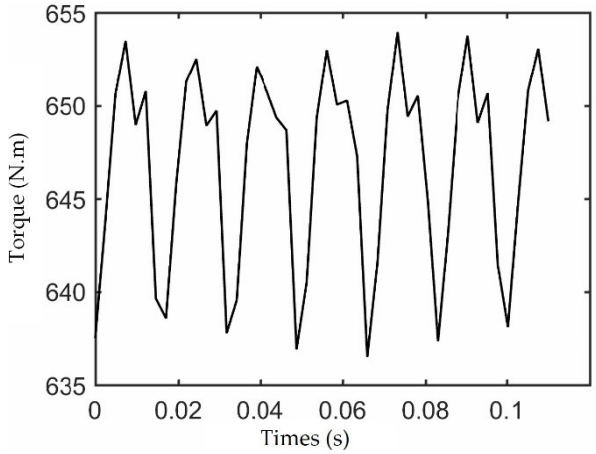

FIGURE 13. Output torque of the prototype motor.

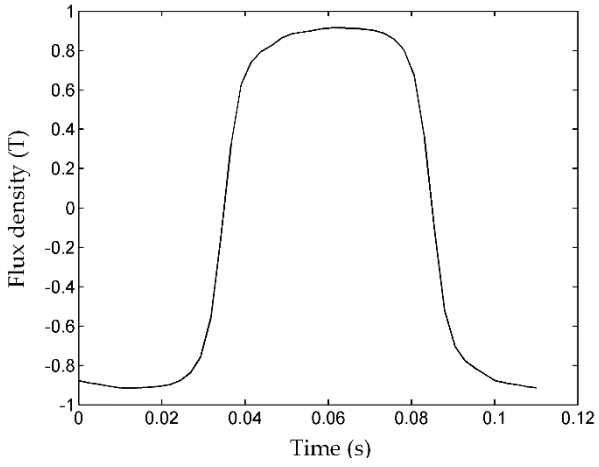

FIGURE 14. Gap flux density.

the fundamental frequency is 10 Hz and the amplitude is 1.05 T; these values are mainly affected by the second and third harmonics. The other harmonics have lower amplitudes.

B. DESIGN OF THE CONTROL SYSTEM

The system comprises three main modules, namely the host computer, motion controller, and motor driver. One

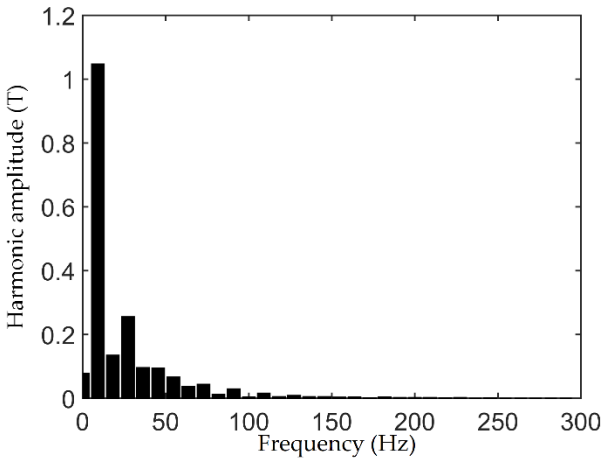

FIGURE 15. Gap flux density spectrum.

communication module in the motion controller, one drive module in the motor driver, and one winding in the motor constitute each redundancy.

The motion controller comprises a motion control module, magnetic encoder module, and multiple communication modules. The motion control module uses a serial peripheral interface communication to receive commands from the host computer and position data from the encoder module. It then calculates the real-time speed or position instructions and sends the instructions to the encoder module.

The magnetic encoder module receives data from a Hall-effect sensor, calculates the position data, and sends the position data to the motion control module. It also receives instructions from the motion control module and sends them to all the communication modules synchronously. Feedback from the motor driver is also sent to the motion control module through the encoder.

Because of the limited number of communication ports in a central processing unit, the system needs multiple communication modules to receive instructions and send them to the corresponding redundant motor drivers. Each module has a tri-gate to ensure that only one redundancy's feedback is sent to the encoder module at a time.

The motor driver has multiple independent driver modules. Each module receives instructions from the communication module and runs the current loop, outputting a pulse-width modulation wave to drive the redundancy.

During failure, the current sensor on the fault redundancy's driver detects the feedback current's raising (short-circuit fault) or falling (open-circuit fault), and the central processing unit then stops driving redundancy. The action does not affect the other driver and motion controller. If the failure breaks the driver, the fault redundancy will also stop.

The output of the multi-redundant motor is the sum of the outputs of all redundancies. There will therefore be a torque ripple in the system that reduces the fall in the motor speed after shutting down the fault redundancy. The motion controller can detect the change in speed in real time and adjust the current reference. By increasing the current of other

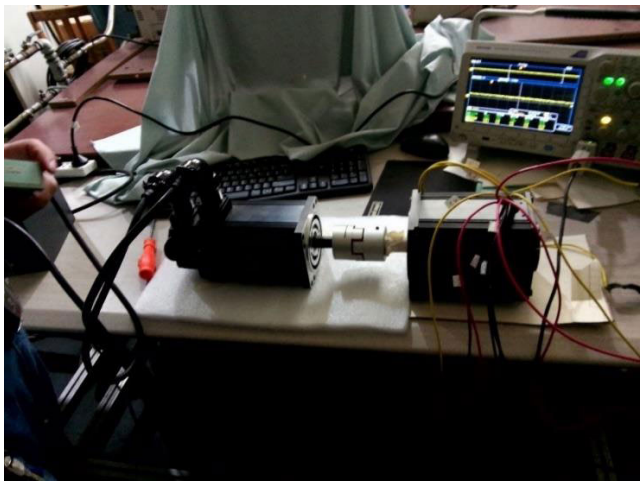

FIGURE 16. Setup for the measurement of the back-emf.

TABLE 3. Results of the back-emf.

	Redundancy 1		Redundancy 2	
Speed (r/min)	Back-emf (V)	Coefficient (V/(r/min))	Back-emf (V)	Coefficient (V/(r/min))
200	8.3	0.0415	10.1	0.0505
400	15	0.0375	16.2	0.0405
800	28.5	0.0356	29.5	0.0369
1000	34.5	0.0345	35.5	0.0355
1500	52	0.0347	52.5	0.035
1800	61	0.0339	61	0.0339

redundancies, the output can be recovered and the ripple can be eliminated.

IV. EXPERIMENTS

A. EXPERIMENT ON MOTOR CHARACTERISTICS

To save time, the motor used in the experiments had two redundancies. A test motor was used to measure the back- emf by imposing drag on the multi-redundant motor at different speeds. The setup is shown in Fig. 16.

Experimental data are given in Table 3. The data in the table were used to visualize the relationship between the speed and back-emf, as shown in Fig. 17.

Fig. 17 shows that back-emf coefficients for redundancies 1 and 2 tend to become uniform with increasing speed, and the linearity is adequate. The induced emf waveforms of the two redundancies, which are shown in Fig. 18, are basically coincident. This reveals that the back-emf characteristics of the two redundancies basically remain consistent.

The motor-locked rotor output torque was measured by changing the current command. The experimental results are listed in Table 4 and plotted in Fig. 19.

Fig. 19 shows that the static torque increases as command current increases, and the static torque coefficient had good consistency.

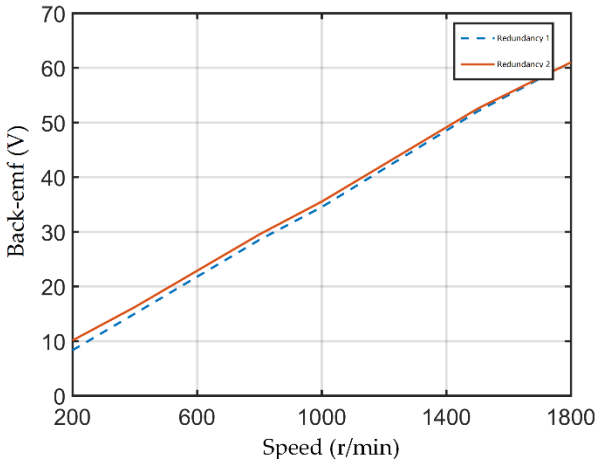

FIGURE 17. Speed versus back-emf for the prototype motor.

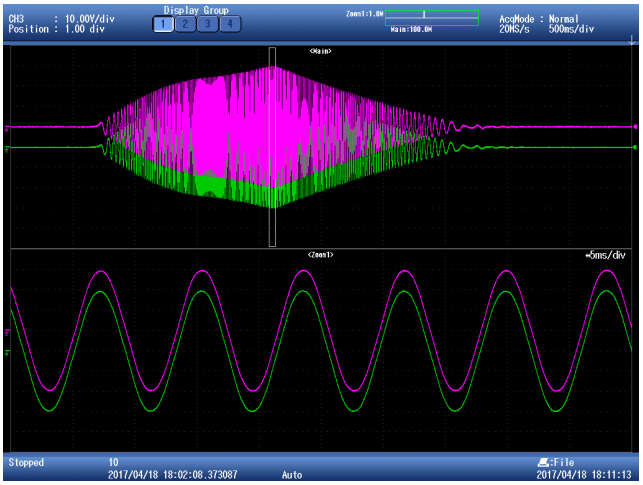

FIGURE 18. Waveform of the back-emf for the prototype motor.

TABLE 4. Results for static torque.

	Redundancy 1		Redundancy 2	
Current (A)	Static torque (N·m)	Coefficient (N·m/A)	Static torque (N·m)	Coefficient (N·m/A)
0	0	/	0	/
5	0.55	0.1100	0.62	0.1240
7.5	1.21	0.1613	1.25	0.1667
10	1.65	0.1650	1.67	0.1670
12.5	2.31	0.1848	2.20	0.1760
15	3.00	0.2000	3.04	0.2027
17.5	3.79	0.2166	3.68	0.2103

The consistency of the back-emf coefficients and static torque coefficients of the two redundancies shows that the characteristics of the two redundancies are consistent. It also shows that the relationship between the motor output torque and the number of redundancies is linear.

B. TEST DRIVING OF THE MULTI-REDUNDANT MOTOR

The platform for the driving experiment is shown in Fig. 20.

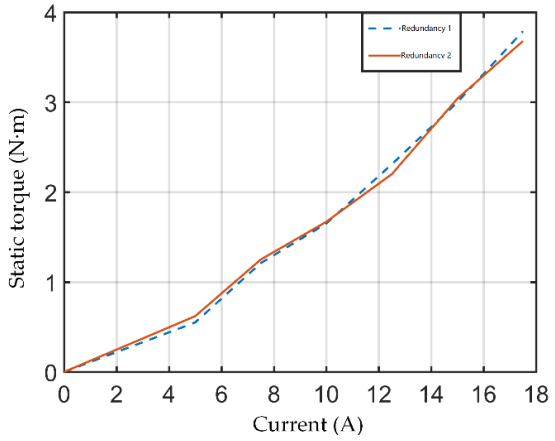

FIGURE 19. Static torque versus current for the prototype motor.

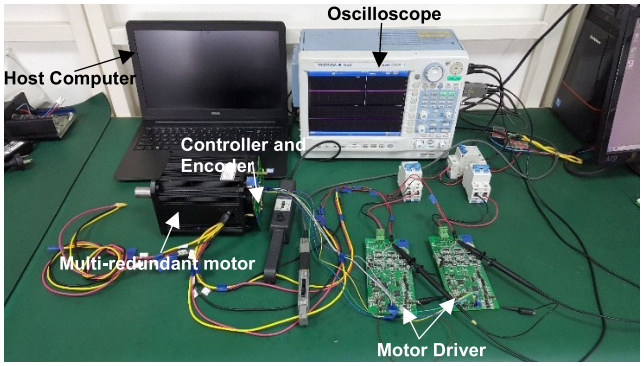

FIGURE 20. Setup of the driving experiment.

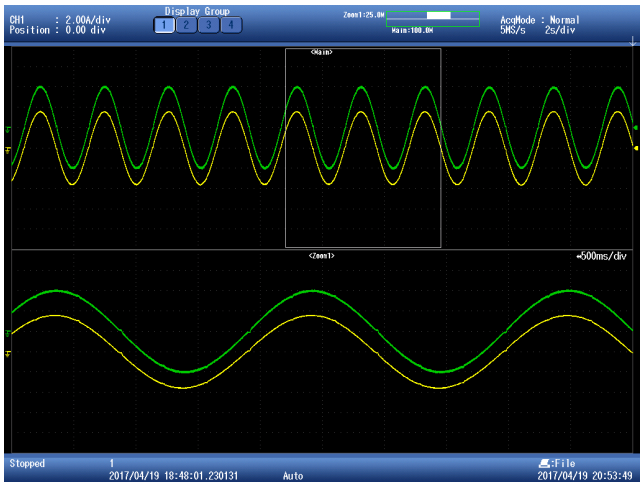

FIGURE 21. Waveforms of the prototype motor current without the encoder.

First, the system was driven without a magnetic encoder to ensure that the redundant windings were synchronous. Two redundant U-phase current waveforms were collected using two probes. The waveforms are shown in Fig. 21.

Fig.21 shows that the two redundancies work well together, with there being stationary and consistent waveforms for both phase and amplitude. Above all, these results show that

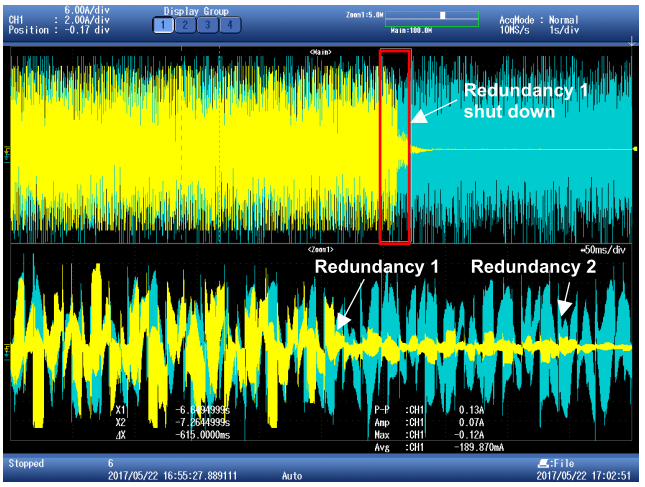

FIGURE 22. Current waveforms during a fault.

the system works normally when driven by two redundant windings.

Next, the two redundancies were driven with the same parameters. During operation, redundancy 1 was powered off to simulate the situation of one redundancy failure. Powering off redundancy 1 is equivalent to shutting down the output voltage of redundancy 1. This situation has the same effect as a failure in the armature winding, inverter, or driving circuit.

Fig.22 shows the U-phase current waveforms of both redundancies during the experiment. When redundancy 1 was turned off, its U-phase current fell to 0 A after a short shock. Redundancy 2 still output current normally and simultaneously. The waveforms show that the system continues operating normally under failure of the armature winding, inverter, or driving circuit.

In this experiment, the back-emf and static torque of each redundancy were tested firstly to show that each redundancy has basic consistent characteristics. The two redundancies were then driven synchronously with the same controller and same parameters. Results show that the multi-redundant PMSM system was controllable. Finally, the driver of one redundancy was shut down to simulate a failing situation, and waveforms showed that the other redundancies continued working normally during and after failure.

V. CONCLUSION

A new multi-redundant PMSM was proposed. First, the controllability of the mutual inductance winding was shown. A mathematical model for the multi-redundant PMSM was then built, and its fault-tolerance performance was demonstrated through simulation. The structure and drive system of the motor were then designed. Finally, an experimental platform was built, and the system's fault-tolerance performance was verified by powering off one redundancy as the motor was operating. The experimental results show that the multi-redundant PMSM continued to work when one redundant winding failed. Compared with other fault-tolerant motor systems, the proposed PMSM system uses normal PI control

theory, has no additional complex algorithm, and has no specific component for controller or drivers. The redundant windings are in parallel with others so the need to bus voltage could be low. The hardware of the control system is easy to downsize and integrate because the controller and driver are independent and divided. The system is suitable for situations that require a shorter control cycle, higher system frequency, lower bus voltage, and a smaller controller and drivers.

REFERENCES

[1] O. Dieterle, T. Greiner, and P. Heidrich, "Control of a PMSM with quadruple three-phase star-connected windings under inverter short-circuit fault," *IEEE Trans. Ind. Electron.*, vol. 66, no. 1, pp. 685–695, Jan. 2019.

[2] Y. Luo and C. Liu, "Pre- and post-fault tolerant operation of a six-phase PMSM motor using FCS-MPC without controller reconfiguration," *IEEE Trans. Veh. Technol.*, vol. 68, no. 1, pp. 254–263, Jan. 2019.

[3] W. Huang, W. Hua, F. Chen, F. Yin, and J. Qi, "Model predictive current control of open-circuit fault-tolerant five-phase flux-switching permanent magnet motor drives," *IEEE J. Emerg. Sel. Topics Power Electron.*, vol. 6, no. 4, pp. 1840–1849, Dec. 2018.

[4] X. Zhou, J. Sun, H. Li, and X. Song, "High performance three-phase PMSM open-phase fault-tolerant method based on reference frame transformation," *IEEE Trans. Ind. Electron.*, vol. 66, no. 10, pp. 7571–7580, Oct. 2019.

[5] G. Liu, L. Qu, W. Zhao, Q. Chen, and Y. Xie, "Comparison of two SVPWM control strategies of five-phase fault-tolerant permanent-magnet motor," *IEEE Trans. Power Electron.*, vol. 31, no. 9, pp. 6621–6630, Sep. 2016.

[6] H. Zhou, W. Zhao, G. Liu, R. Cheng, and Y. Xie, "Remedial field-oriented control of five-phase fault-tolerant permanent-magnet motor by using reduced-order transformation matrices," *IEEE Trans. Ind. Electron.*, vol. 64, no. 1, pp. 169–178, Jan. 2017.

[7] L. Zhang, Y. Fan, R. Cui, R. D. Lorenz, and M. Cheng, "Fault-tolerant direct torque control of five-phase FTFSCW-IPM motor based on analogous three-phase SVPWM for electric vehicle applications," *IEEE Trans. Veh. Technol.*, vol. 67, no. 2, pp. 910–919, Feb. 2018.

[8] S. C. Rangari, H. M. Suryawanshi, and M. Renge, "New fault-tolerant control strategy of five-phase induction motor with four-phase and three-phase modes of operation," *Electronics*, vol. 7, no. 9, p. 159, Aug. 2018. doi: 10.3390/electronics7090159.

[9] A. K. M. Arafat and S. Choi, "Optimal phase advance under fault-tolerant control of a five-phase permanent magnet assisted synchronous reluctance motor," *IEEE Trans. Ind. Electron.*, vol. 65, no. 4, pp. 2915–2924, Apr. 2018.

[10] H. Zhou, G. Liu, W. Zhao, X. Yu, and M. Gao, "Dynamic performance improvement of five-phase permanent-magnet motor with short-circuit fault," *IEEE Trans. Ind. Electron.*, vol. 65, no. 1, pp. 145–155, Jan. 2018.

[11] L. Cheng, Y. Sui, P. Zheng, P. Wang, and F. Wu, "Implementation of post-fault decoupling vector control and mitigation of current ripple for five-phase fault-tolerant pm machine under single-phase open-circuit fault," *IEEE Trans. Power Electron.*, vol. 33, no. 10, pp. 8623–8636, Oct. 2018.

[12] Y. Sui, P. Zheng, Z. Yin, M. Wang, and C. Wang, "Open-circuit fault-tolerant control of five-phase PM machine based on reconfiguring maximum round magnetomotive force," *IEEE Trans. Ind. Electron.*, vol. 66, no. 1, pp. 48–59, Jan. 2019.

[13] N. Ali, Q. Gao, C. Xu, P. Makys, and M. Stulrajter, "Fault diagnosis and tolerant control for power converter in SRM drives," *J. Eng.*, vol. 2018, no. 13, pp. 546–551, Nov. 2018.

[14] Y. Hu, C. Gan, W. Cao, J. Zhang, W. Li, and S. J. Finney, "Flexible fault-tolerant topology for switched reluctance motor drives," *IEEE Trans. Power Electron.*, vol. 31, no. 6, pp. 4654–4668, Jun. 2016.

[15] G. Han, H. Chen, and X. Shi, "Modelling, diagnosis, and tolerant control of phase-to-phase fault in switched reluctance machine," *IET Electr. Power Appl.*, vol. 11, no. 9, pp. 1527–1537, Nov. 2017.

[16] M. Ma, R. Wang, F. Li, J. Wang, and S. Yang, "A fault-tolerant control strategy for switched reluctance motor drive for electric vehicles under short-fault condition," *Microelectron. Rel.*, vols. 88–90, pp. 1221–1225, Sep. 2018.

[17] W. Yang, B. Gou, Y. Lei, and J. Wang, "Short switch fault diagnosis method for power converter using a model-based approach in switched reluctance motor drives," *J. Eng.*, vol. 2019, no. 16, pp. 2137–2141, Mar. 2019.

TONG FENG received the B.Sc. degree from the Harbin University of Science and Technology, China, in 2010, and the M.Sc. degree from Nottingham Trent University, U.K., in 2012. He is currently pursuing the Ph.D. degree with the Harbin Institute of Technology, China. His research interests include permanent magnet synchronous motor servo systems, its communication, and position sensor.

SHUANGHUI HAO was born in Guizhou, China, in 1963. He received the B.Sc. degree from Tianjin University, in 1985, and the M.Sc. and Ph.D. degrees from the Kyushu Institute of Technology, Japan, in 1997. He then began his research on special motor with the Shanghai Electrical Apparatus Research Institute, China. He went to YASKAWA Electric Corporation, Japan, and worked on AC servo motor. In 2003, he began to work with the Harbin Institute of Technology, where he is currently a Professor. He is the author of more than 100 articles, and has more than 60 patents. His research interests include magneto-electric encoder, AC servo systems, numerical control, and signal processing.

XIUWEN ZHANG received the B.Sc. and M.Sc. degrees from the Harbin Institute of Technology, China, in 2011 and 2015, respectively. His research interests include the CNC circuit and control theory.

TIANHONG YANG received the B.Sc. degree from Northeast University, China, in 2016, and the M.Sc. degree from the Harbin Institute of Technology, China, in 2018. His research interests include motor structure and magneto-electric encoder.

LEI WANG received the B.Sc. degree from the Harbin University of Commerce, China, in 2009, and the M.Sc. and Ph.D. degrees from the Harbin Institute of Technology, China, in 2011 and 2015, respectively. He is currently a Lecturer with the Harbin University of Science and Technology. His main research interests include control theory and its application in motor systems, and high precision magneto-electric encoder.